AIAA AVIATION Forum
August 2-6, 2021, VIRTUAL EVENT
AIAA AVIATION 2021 FORUM

10.2514/6.2021-2154

Towards large-eddy simulations of supersonic jets from twin rectangular nozzle with plasma actuation

Guillaume A. Brès*,
Cascade Technologies Inc., Palo Alto, CA 94303, USA
Brandon C. Y. Yeung†, and Oliver T. Schmidt‡,
University of California San Diego, La Jolla, CA 92093, USA
Ata Esfahani§, Nathan Webb¶, and Mo Samimy‖
Ohio State University, Columbus, OH 43210, USA
and
Tim Colonius**
California Institute of Technology, Pasadena, CA 91125, USA

Large-eddy simulation of a jet issuing from rectangular nozzles of aspect ratio 2 is performed. The nozzles are operating at their nominal design Mach number of 1.5. This operating condition and the geometry match those of the companion experiment conducted at Ohio State University. The preliminary results show good agreement with near-field and far-field noise measurements in terms of broadband levels and predictions of screech tone frequencies and amplitudes. In particular, the main noise radiation towards the aft angles and the overall sound pressure level directivity are within 1dB for most relevant frequencies and angles. For future simulations of active control, a numerical model of a localized arc filament plasma actuator is implemented and tested in a small test domain inside one of the nozzles. A grid resolution study is conducted to investigate the minimum grid resolution required for correct energy transport within the boundary layer.

Nomenclature

c	Speed of sound	P	Period
D_e	Area-based equivalent nozzle diameter	r	Radial coordinate
dt	Time step	r_0	Plasma filament radius
f	Frequency	Re	Reynolds number
h	Nozzle height	S	Energy source term
I	Current	St	Strouhal number fD_e/U_j
l, m, n	Spatial and temporal distribution	T	Temperature
L	Plasma filament length	t	Time
M	Mach number	U_j	Mean streamwise jet velocity
NPR	Nozzle pressure ratio	V	Voltage
NTR	Nozzle temperature ratio	w	Nozzle width
p	Pressure	z_l, z_r	Plasma filament boundary coordinates

*Director of Operations; Senior Research Scientist - Aeroacoustics
†Graduate Student, Department of Mechanical and Aerospace Engineering.
‡Assistant Professor, Department of Mechanical and Aerospace Engineering, Senior Member AIAA.
§Graduate Student, Dept. of Mechanical and Aerospace Engineering
¶Research Scientist, Dept. of Mechanical and Aerospace Engineering
‖Professor, Dept. of Mechanical and Aerospace Engineering
**Professor, Dept. of Mechanical Engineering

Δ	Grid spacing	t	Total (stagnation) property
ϕ	Azimuthal angle	j	Fully-expanded jet conditions
ρ	Density	act	Plasma actuator property
σ	Sharpness parameter	i, f	Signal 'on', 'off'
θ	Polar angle	r	Signal rise time

Subscript

∞	Free-stream property

I. Introduction

It is well established that large-scale structures in jets are amenable to excitation and control through dynamic forcing, and such control has been used successfully to achieve flow-based objectives such as mixing enhancement. In contrast, control of noise has proven relatively less successful. Early studies are reviewed by Brown[1] and Henderson.[2] Following exhaustive trial and error approaches, the most successful studies to-date have demonstrated modest noise reductions of 2–3 dB, sometimes over limited frequency ranges.

Studies employing passive devices such as chevrons[3–5] or steady "microjets"[6] also achieve 2–3 dB over low frequencies and, when well designed, suffer little or no penalty at higher frequencies. While they lead to higher spreading of the mean flow, presumably by introducing smaller-scale turbulence structures such as streamwise vortices into the jet shear layers, there appears to be no generally accepted theory of the mechanisms by which these devices reduce sound.

Active control actuators, when operated at frequencies much higher than the peak instability wave frequency ($0.1 < St < 0.5$) (also referred as jet column or jet preferred mode), or when introducing smaller azimuthal structures (e.g. unsteady microjets), may therefore work through a similar mechanism of suppression of instability-wave growth rates. From the wide range of active flow control devices developed in the past,[7] we focus on a specific type of plasma actuators called localized arc filament plasma actuators (LAFPAs) by Samimy et al.,[8] that were found to be particularly well suited to actuate high-speed, high-Reynolds-number flows using high-amplitude and high-frequency local thermal perturbations. Utkin et al.[9] measured the intense rapid localized heating induced by LAFPAs, and modeled it using a one-dimensional arc filament model, where the axisymmetric Navier-Stokes equations include a cylindrical heat source. Kleinman et al.[10] extended the cylindrical heat source to two dimensions. Kim et al.[11] in turn extended the heat source to three dimensions, inside an axisymmetric nozzle.

The present study adapts the plasma actuation modeling strategy proposed by Utkin et al.[9] and employed by Kim et al.,[11] then applies it to a twin rectangular nozzle geometry corresponding to an experimental setup at Ohio State University (OSU). This study is part of a larger effort to exploit large eddy simulation (LES) and data-driven techniques, in pursuit of fundamental understanding of jet noise actuation as well as high-fidelity modeling of complex nozzle geometries with actuation. As a first step, a single initial LES is performed for the twin rectangular nozzle configuration at the baseline (i.e., no plasma actuation) conditions without prior knowledge of the experimental data. In parallel, the modeling of plasma actuation is investigated on a canonical case relevant to the twin jet case. The preliminary jet results and plasma modeling are presented in the next sections.

II. Jet configuration and numerical setup

A. Experimental setup

An experiment has been designed and fabricated at the Gas Dynamics and Turbulence Laboratory at OSU to study the flow physics, aeroacoustics, and active flow control of closely-spaced supersonic twin rectangular jets. The jet facility is located within a 6.2 m $\times$ 5.6 m $\times$ 3.4 m chamber covered with fiberglass wedges and is designed to have a cut-off frequency of 160 Hz. High-pressure air is supplied by three five-stage reciprocating compressors that store the air in two 43 m^3 cylindrical tanks at a maximum pressure of 16 MPa. The air is then dried, filtered and passed through a series of screens in the jet's settling chamber before being fed to the jet plenum. As shown in Figure 1, the twin nozzle assembly is attached to the plenum using a circular mounting plate to allow for adjustment of the azimuthal angle ϕ of the nozzle assembly with respect to the far-field microphone array in 15° increments. The facility is capable of heating the air in the stagnation chamber up to a total temperature ratio (TTR) of 2.5.

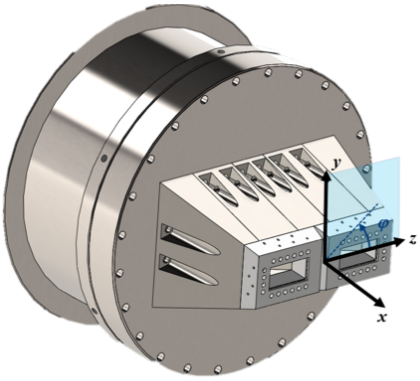

Figure 1. Twin jet assembly showing minor axis y, major axis z, and azimuthal angle ϕ (from Esfahani *et al.*[12])

An array of experimental diagnostics is used for detailed flow and acoustic measurements in both baseline and actively controlled cases. They include velocity measurements on various planes parallel to the major and minor axes of the jets, schlieren imaging, near-field acoustic measurements using a near-field microphone array on a plane located at the nozzle exit to study jet coupling, near-field pressure/acoustic measurements using a linear microphone array that can be translated in both radial and streamwise directions, and far-field acoustic measurements using a microphone array covering a large polar angle range. The present preliminary study focuses on the comparisons with the nozzle-exit and far-field microphone arrays, as shown in figure 2. Additional details about the facility and experiments can be found in Esfahani *et al.*.[12] In the wind-tunnel, the twin-jet nozzle assembly is installed inside a co-flow channel which is not active for this configuration and not included in the computational domain.

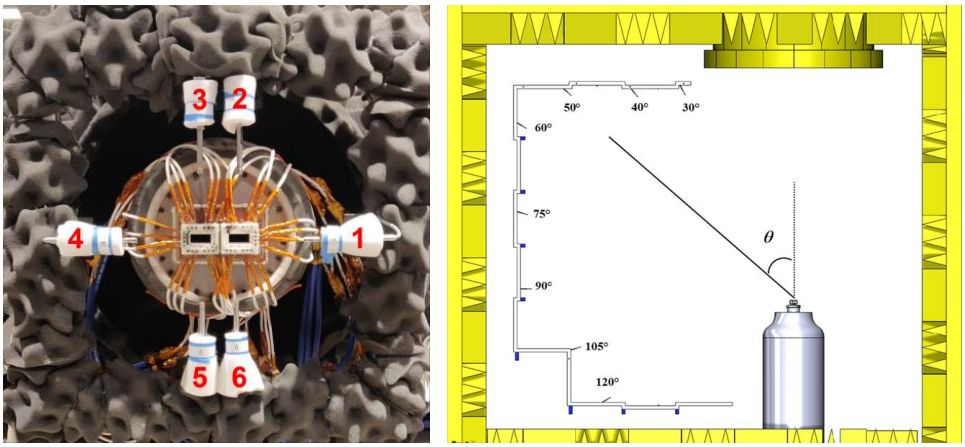

(a) nozzle-exit microphones (b) far-field microphones

Figure 2. Photograph of the near-field nozzle-exit microphone array and schematic of far-field microphone array with polar angle θ (from Esfahani *et al.*[12]).

Each of the plasma actuators used for active flow control consists of a pair of tungsten electrodes that are connected to an output channel of an in-house built arc generator. When triggered, the arc generator ramps up the voltage to about 7 kV at which point the air in the gap between the electrodes breaks down and an arc is formed. The repetition frequency of each actuator can be independently controlled up to 20 kHz. When actuated with a predetermined frequency, the plasma actuators generate thermal perturbations that excite Kelvin-Helmholtz instabilities in the shear layer of the jets.[13] Boron nitride is used for the diverging section of the nozzles to house the plasma actuators to prevent arcing to metal parts. In order to shelter the arc discharge between electrodes, 1 mm wide by 0.5 mm deep grooves were cut into the boron nitride block, approximately 1 mm upstream of the nozzle exit plane, to house the 1 mm diameter tungsten electrodes of the actuators.[8,14]

Previous work[15] has shown that the groove does not affect the control authority of the actuators. Six actuators are placed along the major axis of the nozzle, three on top and three on the bottom, while two actuators are placed along the minor axis of the nozzle. The electrodes for each actuator are arranged such that their tips are approximately 3 mm apart.

B. Nozzle and plasma actuator geometries

Each rectangular nozzle is a bi-conical nozzle with a sharp throat and design Mach number $M_d = 1.5$, height $h = 12.065$ mm and aspect ratio width-to-height $AR = w/h = 2$. The area-based equivalent nozzle diameter D_e is defined as the diameter of a circular jet whose exit area is the same as the rectangular cross-section. The value is $D_e = 19.25$ mm, or $D_e/h = 1.6$, which is also the twin jet spacing, i.e., the inner distance between the nozzle sidewalls at the exit. The center-to-center spacing between the nozzles is therefore $2.25D_e$.

In terms of CAD modifications, a variety of bolt holes and internal structures in the trapezoidal nozzle support have been filled, though the cutouts remain (see Figure 3(b)). Additionally the electrode internal passages have been filled as well as the seams between the two nozzle pieces. The internal groove upstream of the nozzle exit is unchanged. The tips of the tungsten electrodes in the groove are modeled as cylinders flush with the nozzle internal wall such that there is no penetration into the flow (see Figure 3(c)). Additional details about the geometry are provided in Appendix.

The small features associated with the groove and the electrodes would be challenging to mesh with traditional approaches, whether it is for multi-block structured grids or even generalized unstructured grids (e.g., hexahedral/tetrahedral/prismatic). As these geometrical details are expected to be important for the flow physics and plasma modeling, they are explicitly included in the computational domain thanks to the novel mesh-generation approach based on the computation of Voronoi diagrams described in the next Section II C.

C. Voronoi mesh generation

The Voronoi-based meshing technology developed at Cascade Technologies computes a grid from the specification of the relevant surface geometry and the set of generating points where the solution is to be sampled. A Voronoi diagram uniquely defines a mesh from the prescription of the geometry and point cloud alone, based on Euclidean distance: connectivity and topology are unique and deterministic consequences of the points and surface. This decomposition is illustrated in Fig. 4.

A powerful aspect of using Voronoi diagrams to produce computational meshes is that the definition of the Voronoi vertex locations uniquely describes the Voronoi mesh, including all geometric information (e.g. volumes, face normals and areas), and connectivity (e.g. nearest neighbors). This deterministic connection between the point locations and the resulting mesh simplifies mesh adaptation and manipulation, as well as mesh motion. For example, increasing the point density in a particular region corresponds simply to increasing the number of points in that region, or smoothing the mesh corresponds simply to smoothing the distribution of points, free from impact on mesh connectivity.

The generation of a three-dimensional Voronoi mesh inside a complex fluid volume is essentially a three-step iterative but highly-local computation:

1. Define the generating point set, i.e., the coordinates of the Voronoi vertices that will eventually correspond to the locations of unknowns.

2. Generate the Voronoi diagram, in parallel, from the generating point set including potentially non-convex boundaries.

3. Potentially smooth or refine the mesh by changing the locations of some or all points, and repeat step 2.

One interesting property is that the point cloud and surface are independent objects, i.e., the mesh topology is decoupled from the surface description. The same surface geometry, regardless of tessellation, can be reused during mesh design iterations. Additionally, since the Voronoi diagram is generated solely from point clouds, surfaces can be arbitrarily moved or deformed without folding cell challenges. The Voronoi diagram possesses other desirable properties by construction, e.g., orthogonality of face normal and cell displacement vectors, enabling computational efficiencies for both the mesh generator and fluid solver.

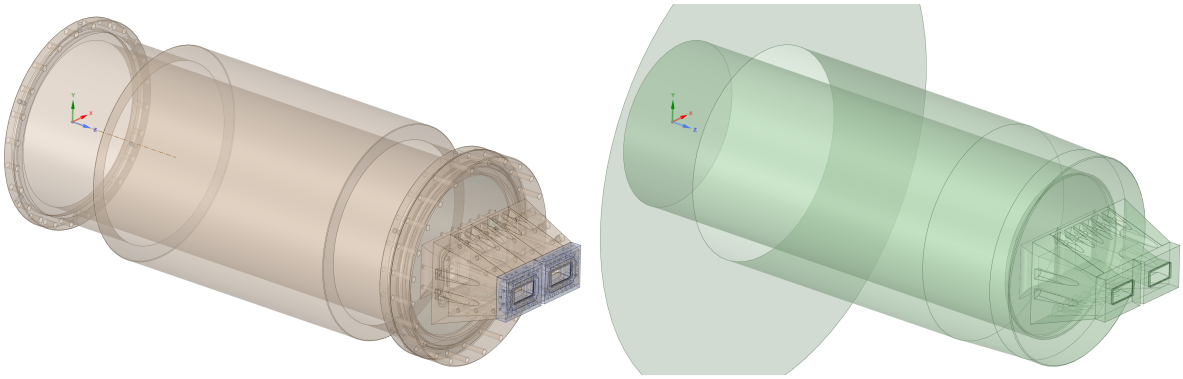

(a) Overview

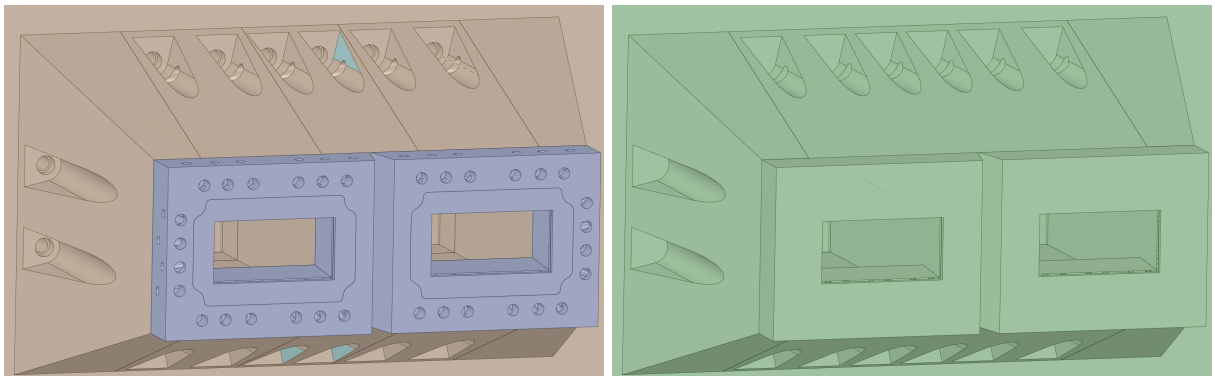

(b) Nozzle exterior

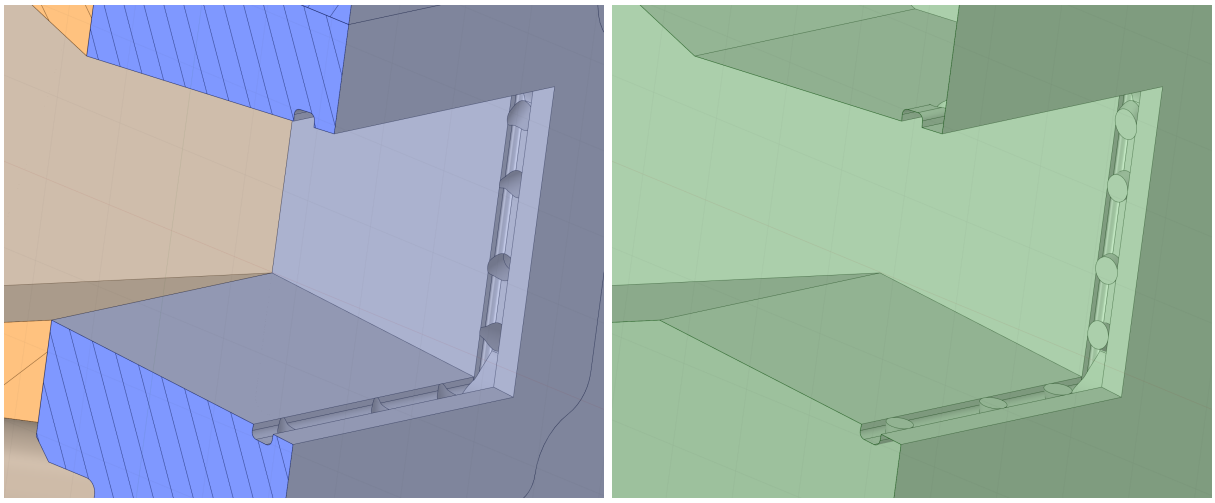

(c) Details of the groove and electrodes near the nozzle exit

Figure 3. Comparison between the hardware description (left) and the wetted (i.e., computational) surface description (right) for various features of the nozzle configuration.

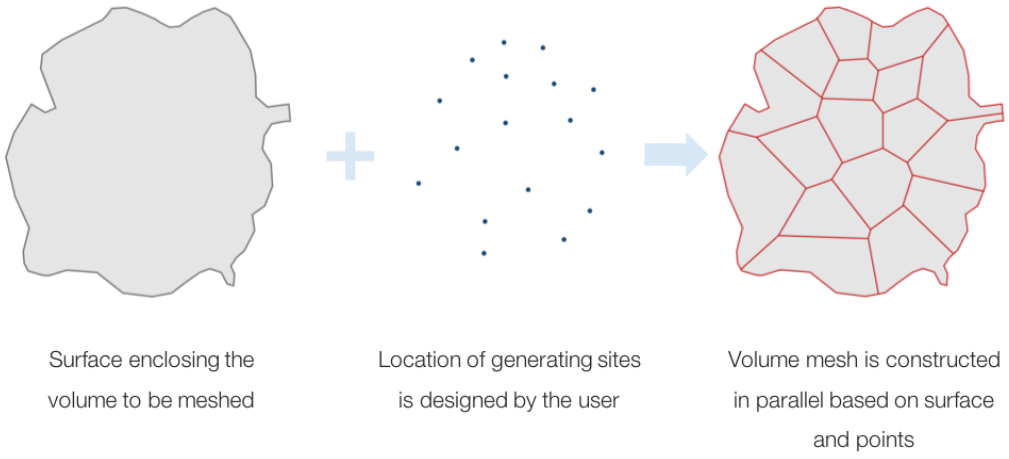

Figure 4. Clipping surface combined with seeding points yields a Voronoi mesh.

The generation of a Voronoi diagram from a point set is normally performed by either computing the Delaunay triangulation and then taking its dual, or by directly computing the Voronoi diagram from its geometric definition.[16] As the generation of the Delaunay triangulation in 3D has problems associated with degenerate point sets, a parallel method has been developed, based primarily on hexagonal close-packed (HCP) point distributions. Hexagonal close-packing refers to the spatial arrangement of points corresponding to stable sphere packing. In this arrangement, points are placed inside the fluid volume of interest using an HCP lattice as a guide when seeding points in the domain.

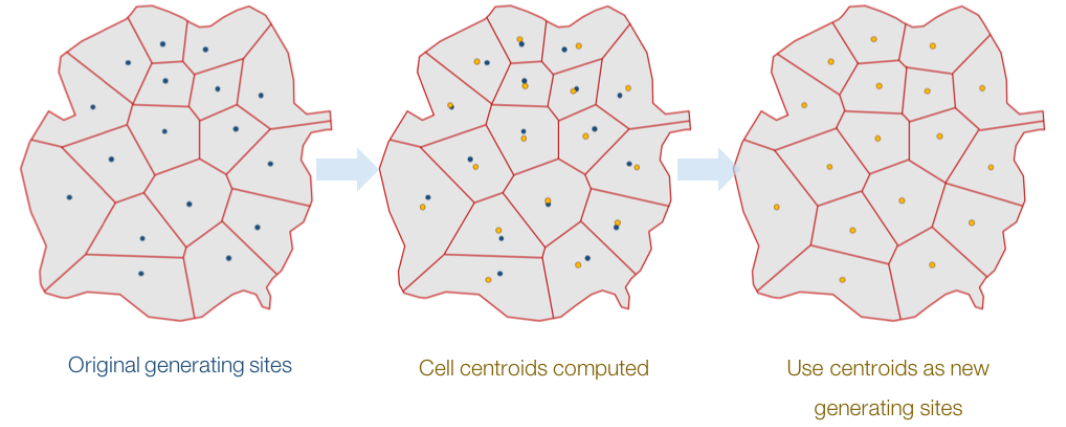

Figure 5. Example of a single Lloyd iteration step.

Another compelling reason for using Voronoi diagrams for meshing is the ability to smooth and iteratively improve the mesh in a robust and stable way. For most traditional meshes, particularly unstructured meshes, smoothing can be a complicated process with few guarantees. Meshes can fold, and modifications to the connectivity are tedious. For Voronoi diagrams, however, the connectivity is directly and uniquely determined from the point locations, so smoothing algorithms need only consider the smoothing of the point locations. One such smoothing algorithm is called Lloyd iteration,[17] as illustrated in Figure 5. Lloyd iteration makes use of the fact that the Voronoi points and the centroids of the resulting Voronoi cells do not necessarily coincide: when they do, the Voronoi mesh is called *centroidal*. In the most basic implementation of Lloyd iteration, the generating points are moved to the centroids of their Voronoi cells, and the Voronoi mesh is recomputed. Lloyd iteration can also be restricted to a subset of the point cloud so that it does not disturb pre-existing point spacing.

D. LES Methodology

The large-eddy simulations are performed using the unstructured compressible flow solver "Charles" developed at Cascade Technologies, Inc. (https://www.cascadetechnologies.com). For the present version of the solver, the mesh is generated through the computation of a Voronoi diagram described in the previous Section II C.

In this initial study, the simulation corresponds to the baseline conditions without plasma actuation. The LES nondimensionalization is based on the nozzle height h and the ambient speed of sound $c_\infty = \sqrt{\gamma p_\infty/\rho_\infty}$. The resulting form of the ideal gas law is $p = \rho T/\gamma$, with constant specific heat ratio $\gamma = 1.4$. The nozzle pressure ratio and nozzle temperature ratio are defined as $NPR = P_t/P_\infty = 3.671$ and $NTR = T_t/T_\infty = 1$, where the subscript t and ∞ refer to the stagnation (total) property and free-stream conditions, respectively. For the present nominally ideally-expanded conditions, the jet is cold ($T_j/T_\infty = 0.69$) and the jet Mach number and acoustic Mach number are defined as $M_j = U_j/c_j = M_d = 1.5$ and $M_a = U_j/c_\infty = 1.25$, where U_j is the mean (time-averaged) streamwise jet velocity and the subscript j refer to the (equivalent) fully-expanded jet properties. The experimental Reynolds number is $Re_j = \rho_j U_j D_e/\mu_j \approx 10^6$ and is matched in the simulations.

The midpoint between the nozzle spacing is at $(0, 0, 0)$, such that the two nozzle exits are centered at $(0, 0, \pm 1.8h)$. As shown in Figure 6(a), the farfield was constructed as a axisymmetric truncated cone, where the diameter grew as the domain extended downstream: the co-flow inlet plane is roughly $30h$ upstream of the nozzle exit, and the outflow is $110h$ downstream. The farfield starts at a radius of $40h$ and grows to a radius of $80h$ at the outflow.

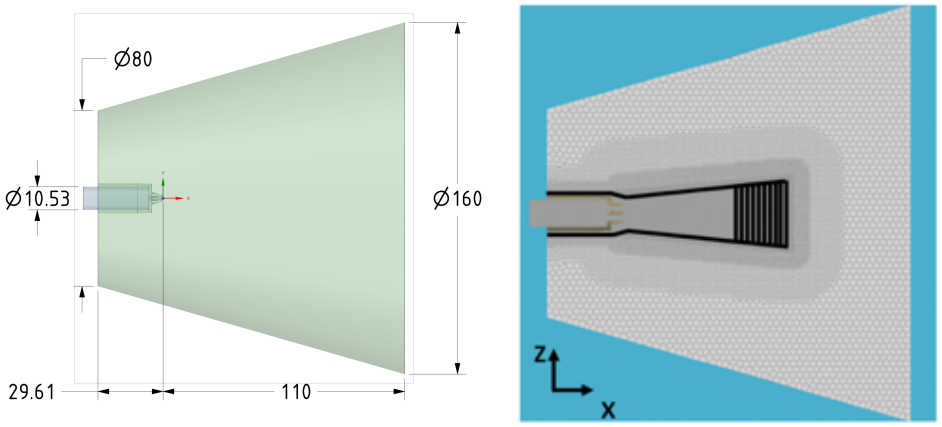

(a) Domain dimension (b) Mesh & FW-H surface

Figure 6. Visualization of the computational domain (dimensions normalized by the nozzle height h), Voronoi mesh and outline of the FW-H surface.

The zones for the majority of the surface are described in Figure 7. The internal passages upstream of each nozzle have been separated at locations where the axial gradient of the duct area changes. This results in two converging sections (at the mouth and after the square duct), a constant area square duct section, and the divergent nozzle portion which is split by the electrode groove. This separation was done to provide more flexibility on the application of local near-wall grid refinement and boundary conditions (e.g., no-slip wall versus wall model). For these zones, there is no distinction between the two nozzles as the same mesh parameters and boundary conditions will be applied on both.

The rest of the numerical setup is similar to previous studies with the Charles solver.[18–21] A very slow coflow at Mach number $M_\infty = 0.01$ is imposed outside the nozzle in the simulation in order to prevent any spurious recirculation and facilitate flow entrainment. Sponge layers and damping functions are applied to avoid spurious reflections at the boundary of the computational domain.[22,23] The Vreman[24] sub-grid model is used to account for the physical effects of the unresolved turbulence on the resolved flow. Along with near-wall grid refinement, wall modelling based on the equilibrium boundary layer assumption[25–27] is applied on the convergent_duct, divergent and divergent_lip zones. The far-field noise is computed using the frequency-domain permeable formulation[28] of the Ffowcs Williams & Hawkings[29] (FW-H) equations. For the treatment of the FW-H outflow disk, the method of "end-caps" of Shur *et al.*[30] is used.

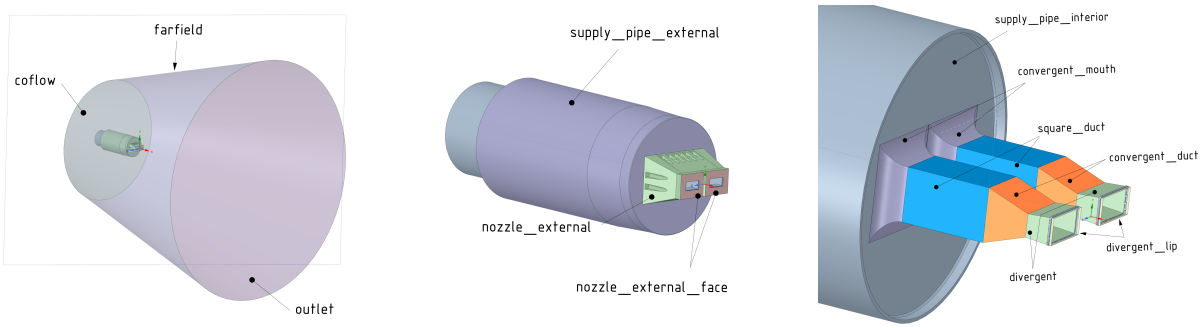

(a) Farfield zones (b) Nozzle external zones (c) Nozzle internal zones

Figure 7. Labeled zones of the computational domain for specification of boundary conditions.

E. Modeling of plasma actuation

This section describes the plasma actuation model, which is identical to the one proposed by Kim et al.[11] Representing the plasma filament that develops between pairs of electrodes, and added to the right-hand side of the energy equation, is a volumetric heat source

$$S(x,y,z,t) = n(t)\, l(r)\, m(z) \frac{VI}{\pi r_0^2 L}\,, \tag{1}$$

with spatial distribution functions

$$l(r) = \frac{1}{2}\left[\tanh\left(-\sigma_{xy}\left(r - \frac{1}{2}\right)\right) + 1\right], \tag{2}$$

and

$$m(z) = -\frac{1}{2}\left[\tanh\left(-\sigma_z \frac{z - z_l}{r_0}\right) + 1\right] + \frac{1}{2}\left[\tanh\left(-\sigma_z \frac{z - z_r}{r_0}\right) + 1\right]. \tag{3}$$

This heat source has the shape of a cylinder of radius r_0, centered in the groove. It is bounded by $z = z_l$ and $z = z_r$ in the axial dimension, and centered at $(x_{\text{act}}, y_{\text{act}})$ so that $r = \sqrt{((x - x_{\text{act}})/r_0)^2 + ((y - y_{\text{act}})/r_0)^2}$. σ_{xy} and σ_z control the sharpness of the boundary that encloses the heat source.

The square-wave signal is given by

$$n(t) = \frac{1}{2}\left[\tanh\left(\frac{t - t_i}{t_{r,i}}\right) - \tanh\left(\frac{t - t_f}{t_{r,f}}\right)\right], \tag{4}$$

where t_i, t_f are the times at which the signal turns 'on' and 'off', and $t_{r,i}$, $t_{r,f}$ are the corresponding rise times.

The plasma actuation model is validated within a flat-plate turbulent boundary layer. The actuator is situated in a groove across the plate, as it is intended to be in the twin jet nozzle. Although the plasma filaments in the nozzle have finite length, here—for simplicity—the test domain has been made spanwise-periodic. This geometry is illustrated in Fig. 8, with dimensions normalized by the groove width. The freestream Mach number is defined as $M_\infty = 1.5$. The Reynolds number based on momentum thickness is defined as $Re_\theta = 31000$. The strength of the actuation is loosely based on values from Utkin et al.:[9] $V = 400$ and $I = 0.25$. The actuator has a radius of $r_0 = 0.25$, and spans the domain such that $z_l = -1.5$ and $z_r = 1.5$. The sharpness parameters are defined as $\sigma_{xy} = \sigma_z = 5$. The actuation period is defined as $P_{\text{act}} = 2$, while the signal 'on', 'off', and rise times are $t_i = 0.4$, $t_f = 0.8$, and $t_{r,i} = t_{r,f} = 0.04$.

Owing to a lack of experimental measurements in the jet nozzle boundary layer, the implementation of the actuation is instead verified by performing a grid resolution study. The mesh is refined along the wall as well as inside the groove, first to match the resolution of the twin jet simulation, then to higher resolutions. As shown below, quantitative comparison of the results from the low- and high-resolution cases provide valuable insights into the influence of the wall model on the actuation, and thus the minimum grid resolution required for correct energy transport along the boundary layer.

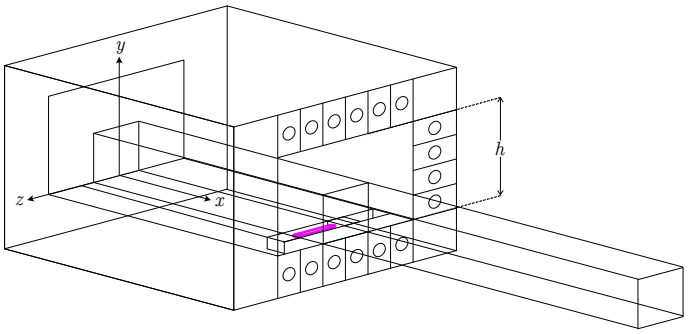

(a) Test domain in relation to jet nozzle

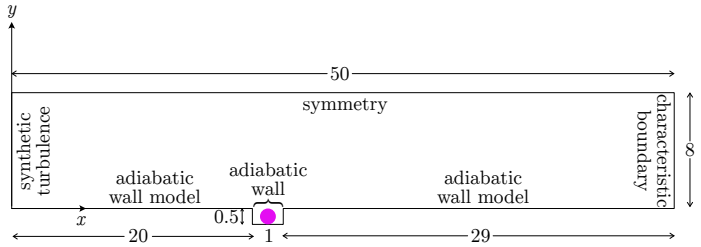

(b) Two-dimensional view of the test domain, with boundary conditions

Figure 8. Computational domain used to analyze the implementation of the plasma model. The magenta cylinder represents a plasma filament. Dimensions are normalized by the groove width.

III. Preliminary results

A. Initial LES of the baseline twin jet configuration

The mesh used for the preliminary simulation is about 65 million cells, with emphasized refinement along the walls and within the shear layer of the jet. The finest resolution is $\Delta = 0.01h$ in the near wall region, including the plasma groove, such that there are approximately 8 control volumes (cv) and 4 cv across the width and depth of the groove. A single baseline LES is performed for the design conditions of the OSU nozzle, without prior knowledge of the experimental data. After the initial transient, the runtime for collection of statistics is $t_{sim}c/h \approx 611$. The simulation time step is $dtc/h = 0.001$, the sampling frequency of the FW-H surface data is $DSt = 12.8$ and the computational cost is approximately 240 kCPUh (i.e., time-to-solution of 36h on 6600 cores.)

Figure 9 shows the visualization of the instantaneous temperature in various planar cuts of the twin rectangular nozzle and jet plume. Recall that the configuration features bi-conical nozzles with sharp throat. Therefore, there are shock waves in the flow even for the present nominally ideally-expanded conditions. Since these nozzles are relatively short and the flow is continuously accelerating within the nozzle, the boundary layer is very thin. However, because of the relatively large Reynolds number and the presence of groove 1 mm upstream of the nozzle exit, the boundary layer at the nozzle exit appears to be turbulent. Additional analysis on the flow statistics and nozzle-exit boundary layer state will be conducted in future work, as part of a grid refinement study.

The main results from the preliminary baseline LES are the FW-H noise predictions in terms of power spectral density (PSD) and overall sound pressure levels (OASPL), which are compared to near-field and far-field microphone measurements in figures 10 and 11, respectively. All the FW-H calculations are performed at the exact location of the experimental microphones. For both the experimental and numerical data, a bin-average PSD is computed as a function of frequency reported in Strouhal $St = fD_e/U_j$, with bin size $\Delta St = 0.025$, and the OASPL are evaluated from $St = 0.05$ to 3.

For the near-field noise in figure 10, the data is presented collectively for the statistically-equivalent microphones 1 & 4 along the major axis, and 2, 3, 5 & 6 along the minor axis (see photograph of nozzle-exit microphones in figure 2(b). The comparison between experiment and LES is good for both the broadband and screech tone components, up to frequency $St \approx 1$. In the higher frequencies, a plateau is observed in

(a) $y = 0$ (i.e., through centerline along major axis)

(b) $z = 1.8h$ (i.e., through centerline along minor axis)

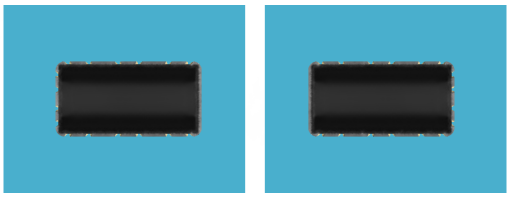

(c) $x = 0$ (i.e., nozzle exit)

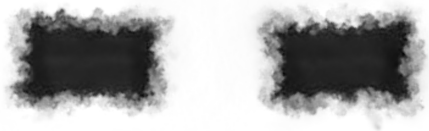

(d) $x = 2h$

(e) $x = 5h$

(f) $x = 10h$

Figure 9. Planar cut of the instantaneous temperature in the twin rectangular nozzle and jet plume: T/T_∞ from 0.65 (black) to 1 (white)

the experimental spectra, while the LES spectra has a more uniform slope and traditional decay rate. The origin of this feature in the measurement data and reasons for its absence in the LES are under investigation. Nevertheless, the main noise sources are well captured in the simulation and the agreement on the OASPL is within 1dB for all microphones. For this configuration, screech is observed with the main tone at $St \approx 0.3$ primarily in minor axis direction, leading to an increase of OASPL of approximately 5dB in that direction.

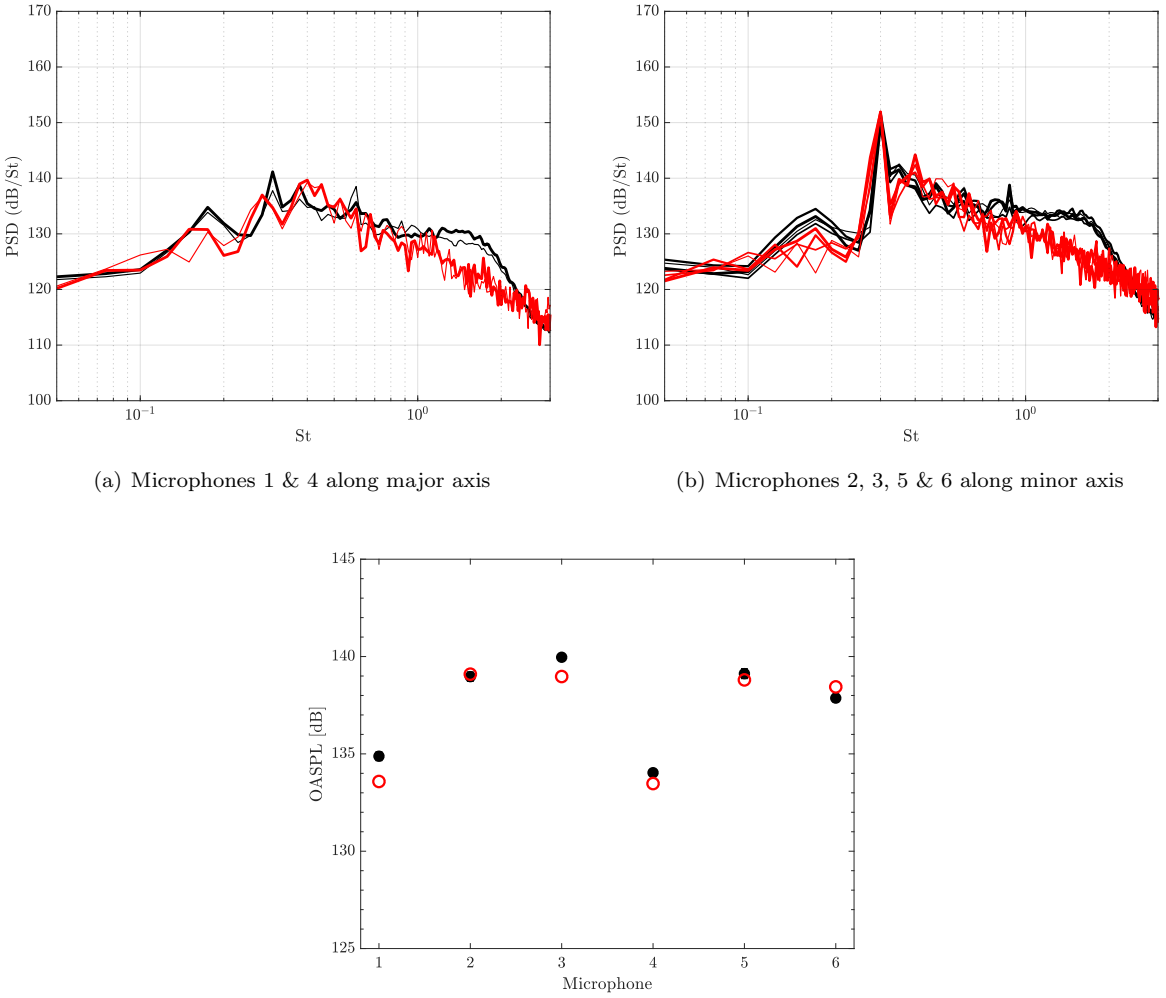

(a) Microphones 1 & 4 along major axis

(b) Microphones 2, 3, 5 & 6 along minor axis

(c) Overall sound pressure levels

Figure 10. Comparison of the experimental (black) and "blind test" LES (red) near-field spectra and OASPL at the nozzle-exit microphones 1 to 6 shown in figure 2(a). The line thickness increases with microphone number.

For the far-field noise in figure 11, a good agreement is again found between experiment and LES, in particular for the aft angles (i.e., $\theta \approx 40°$) along the major and minor axes. As upstream details of to the experimental including acoustic insulation and cabling for the plasma actuators and pressure probes are not part of the numerical setup, a similarly good agreement cannot be expected for the sideline/upstream radiation. Also, the experimental time-history of pressure data is recorded as 400 blocks of 8,192 samples, with sampling frequency $Df = 200$ kHz (i.e., $DSt = 8.9$). The duration of each experimental block is therefore $t_{exp}c/h \approx 1131$, which is nearly twice the duration of the present single block LES data (i.e., $t_{sim}c/h \approx 611$). To reflect on these differences, the block-to-block variation in the short-time-averaged spectra of the long experimental measurements is shown as vertical black line on the figure. These variation are of order ± 0.5 to 1.5 dB for most relevant angles and frequencies. Despite these caveats, the comparison for the sideline/upstream angles (i.e., $\theta \approx 75°$) shows a satisfactory agreement within the experimental block-to-block variations, for all but the highest frequencies, with again a plateau in the experimental spectra

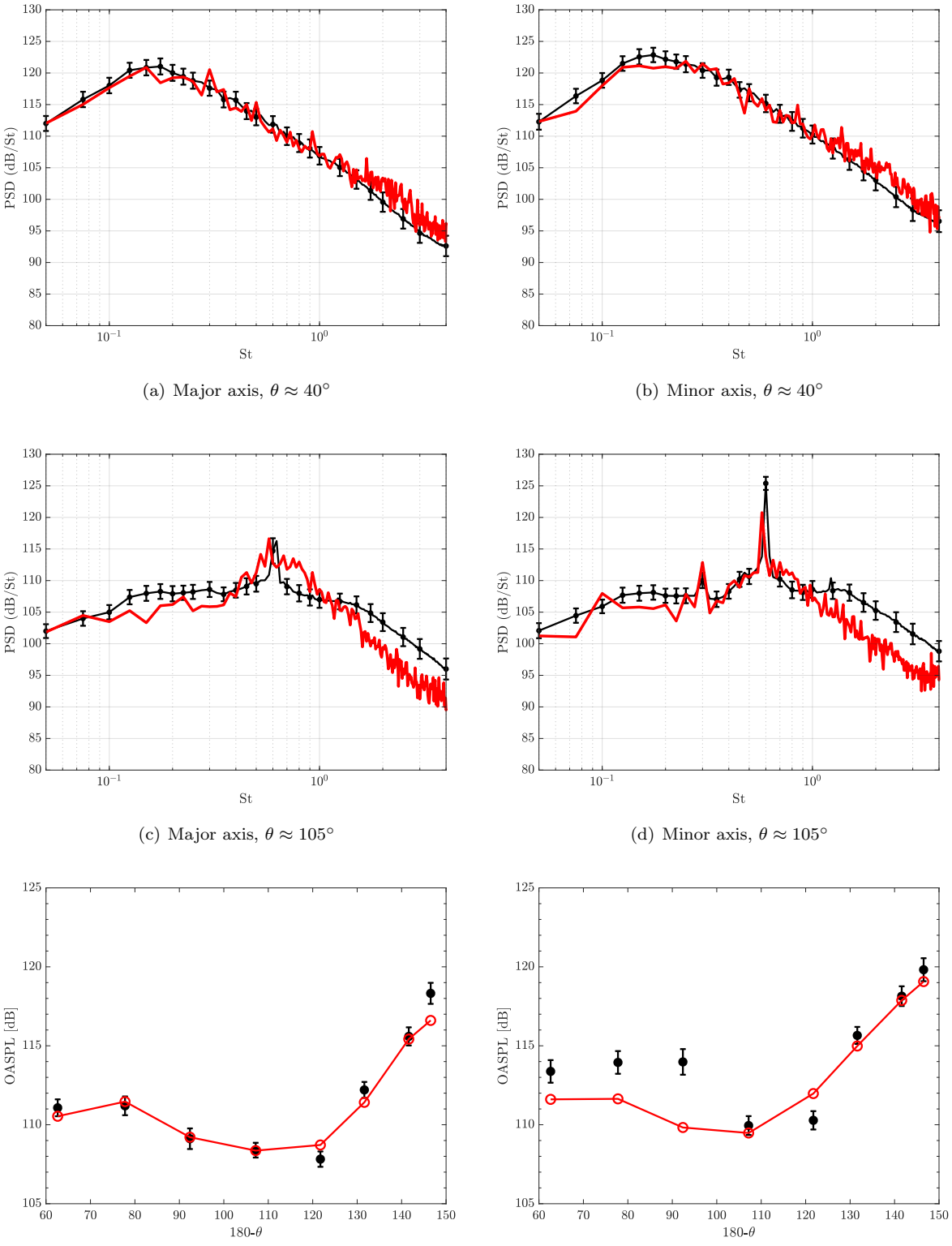

(a) Major axis, $\theta \approx 40°$

(b) Minor axis, $\theta \approx 40°$

(c) Major axis, $\theta \approx 105°$

(d) Minor axis, $\theta \approx 105°$

(e) Major axis, overall sound pressure levels

(f) Minor axis, overall sound pressure levels

Figure 11. Comparison of the experimental (black) and "blind test" LES (red) far-field spectra and OASPL at the experimental microphones shown in figure 2(b). The vertical bars show the block-to-block variations in the short-time-averaged spectra of the long experimental measurements, compared to the 1-block LES prediction.

reminiscent of the one present in the near-field spectra. Again, the distinct peaks in both the experimental and numerical spectra correspond to the screech tone and its super- and subharmonics. Much like for the near-field spectra presented in figure 10, the screech tone is more intense in the minor direction but the main tone in the far-field is now at $St \approx 0.6$ rather than 0.3. Most notably, the prediction of the OASPL (last row) by the present single "blind test" simulation is excellent: along the major axis, the accuracy of the prediction is within the block-to-block variation , with sub-dB difference for all angles but $\theta \approx 30°$. Equally good results are found for the minor axis for the aft angles. For smaller angles, the prediction is still within 2-4 dB.

B. Verification of the plasma model

From the test domain (Fig. 8) used to verify the plasma actuation model, 3 successively refined meshes are constructed. The first mesh, $\Delta_{\min} \approx 0.12$, matches the near-wall resolution of the twin jet simulation, and contains about 0.15 million cells. The second and third, $\Delta_{\min} \approx 0.06$ and $\Delta_{\min} \approx 0.03$, each doubles the resolution of the previous mesh, and have about 0.62 million and 2.5 million cells, respectively. A small region near the groove in each mesh is visualized in Fig. 12.

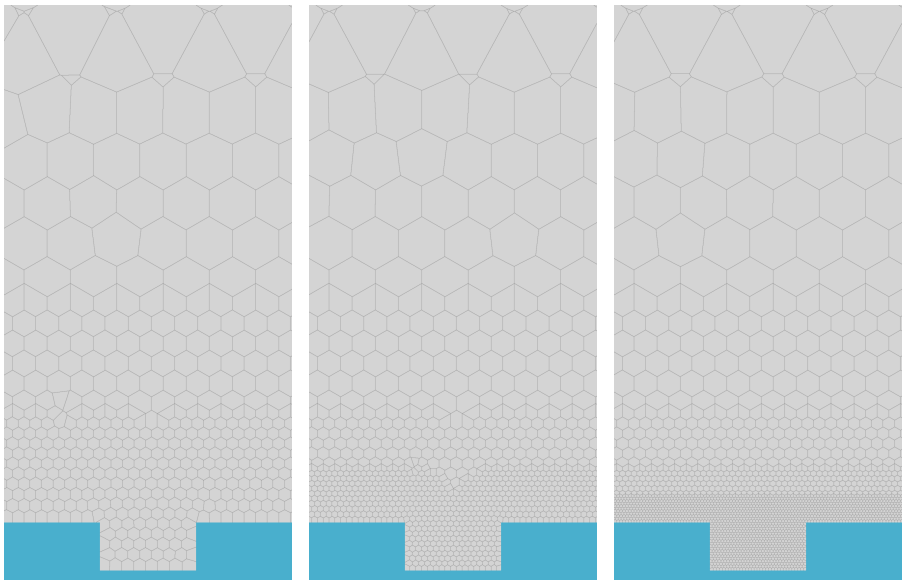

(a) $\Delta_{\min} \approx 0.12$ (b) $\Delta_{\min} \approx 0.06$ (c) $\Delta_{\min} \approx 0.03$

Figure 12. Computational meshes used in the grid resolution study of the simplified test domain. Dimensions are normalized by the groove width. Only a small region enclosing the groove is shown here.

Without the benefit of experimental boundary-layer measurements for direct validation, the $\Delta_{\min} \approx 0.03$ case will be treated as an approximation to the true solution. Although an in-depth investigation of cavity flows is beyond the scope of this work, it should be noted that in the baseline simulation, this resolution is sufficiently high for pressure waves emanating from the trailing edge of the groove—corresponding to Rossiter mode—as well as recirculating vortices within the groove, to be observed, as shown in Fig. 13.

After the initial transients, each simulation is run for 12 actuation periods, at the end of which the first pulse from the actuator has approximately reached the domain outlet. In the highest-resolution case, i.e. $\Delta_{\min} \approx 0.03$, the instantaneous temperature field after 12 periods, averaged along the spanwise direction, is visualized in Fig. 14.

Figure 15(a) plots the spanwise-average temperature and turbulent kinetic energy (TKE) after 12 actuation periods, integrated over wall-normal distance. As expected, both temperature and TKE show the higher-resolution meshes capturing more of the energy injected into the boundary layer by the plasma actuation, with lower dispersive error. In particular, near the actuator, the $\Delta_{\min} \approx 0.03$ and $\Delta_{\min} \approx 0.06$ cases predict prominent peaks in TKE, whereas $\Delta_{\min} \approx 0.12$ shows no peaks in that region. Far downstream of the groove, $\Delta_{\min} \approx 0.12$ remains the lowest in temperature; however, the $\Delta_{\min} \approx 0.03$ and $\Delta_{\min} \approx 0.06$ cases predict very similar temperatures. As an attempt to isolate some of the effects of grid resolution on

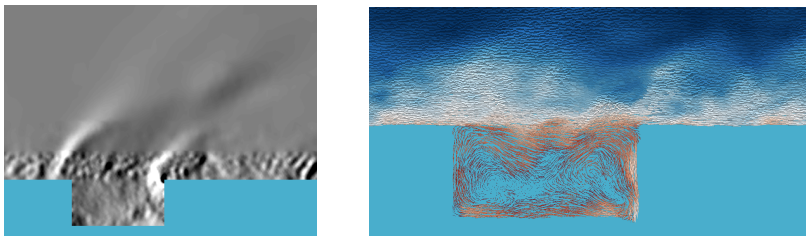

(a) Numerical schlieren, $\partial\rho/\partial x$ (b) Streamlines

Figure 13. Details of the baseline simulation in the $\Delta_{\min} \approx 0.03$ test case, in and around the groove. Streamlines are colored by velocity magnitude.

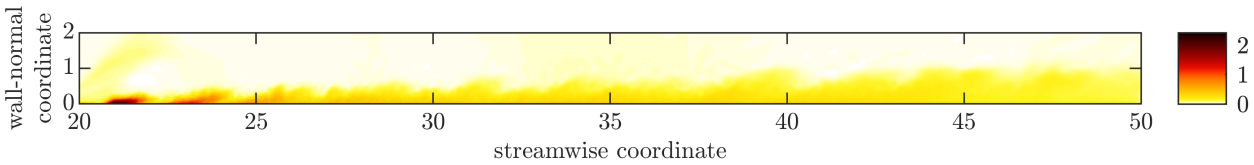

Figure 14. Log of temperature in the highest-resolution test case ($\Delta_{\min} \approx 0.03$) averaged along the spanwise direction, after 12 actuation periods.

the plasma model itself, Fig. 15(b) plots the temperature and TKE, now with the baseline quantities subtracted. As before, close to the actuator, the higher-resolution meshes capture higher temperatures. Away from the actuator however, the temperatures predicted by all 3 cases show close agreement. This suggests that the energy present in the baseline turbulent boundary layer is better captured by finer grids—again as anticipated—but the *additional* energy injected by the plasma, measured in terms of temperature far from the actuator, is much less sensitive to grid resolution. Though the physics near the groove is significantly modified by the larger grid spacings, as long as the region of interest is far downstream of the actuator, these results tentatively suggest that the current refinement level within the nozzle-exit boundary layer of the twin jet case is sufficient. A detailed comparison of temperature and TKE between successively refined meshes requires fully converged solutions, and will be included as part of future work.

IV. Conclusion

As a first step towards modeling plasma actuation in supersonic jets, a Mach 1.5 cold jet issuing from a twin rectangular nozzle of aspect ratio 2 is investigated using large eddy simulation. The operating condition and geometries match the experimental configuration from Ohio State University, including the electrodes and small groove upstream of the nozzle exit to shelter the arc discharge between electrodes during actuation. In the present study, a single initial LES was performed at the baseline conditions (i.e., no plasma actuation) without prior knowledge of the experimental data. The preliminary noise predictions are in good agreement with the near-field and far-field microphone data. The broadband levels, the screech tone frequencies and amplitudes and the main noise radiation towards the aft angles are well predicted. Additional analysis is ongoing to investigate some of the discrepancies for upstream angles and higher frequencies. Nevertheless, the overall sound pressure level directivity from the LES is within 1dB of the experimental value for most relevant frequencies and angles.

In parallel, the modeling of plasma actuation is investigated in the canonical configuration of a flat-plate turbulent boundary layer, with the actuator situated in a groove across the plate, as it is intended to be in the twin jet nozzle. A grid resolution study was conducted to verify the model implementation, and guide the minimum grid resolution required to correctly predict energy transport within the nozzle-exit boundary layer. Preliminary results tentatively suggest that the current resolution in the twin jet case is sufficient.

In future work, the baseline LES will be further analyzed and validated against additional experimental data (including PIV), as it becomes available. Validation of the plasma actuator model in the settings of the twin jet configuration will be performed with the OSU data. For both baseline and actuation cases, full LES databases will then be collected for statistical (SPOD) analysis.

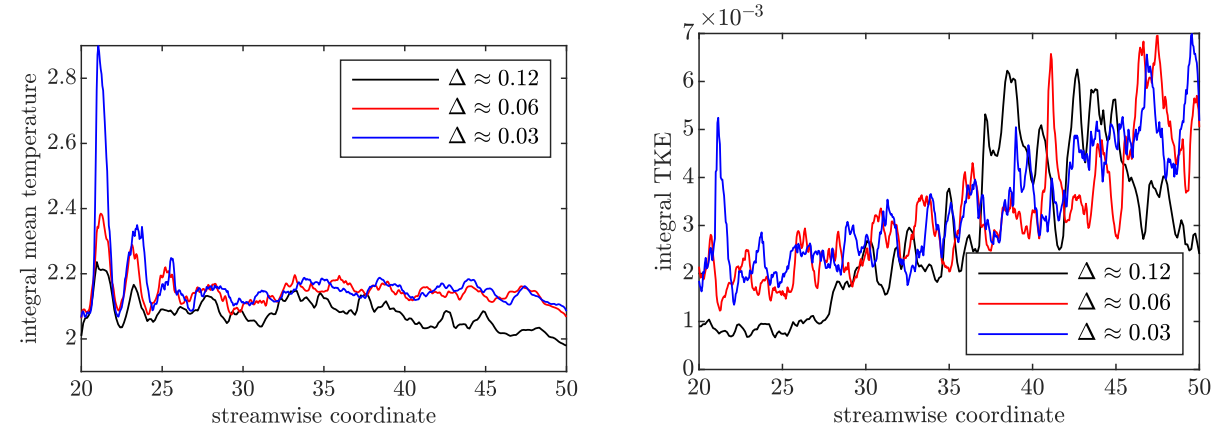

(a) Actuation

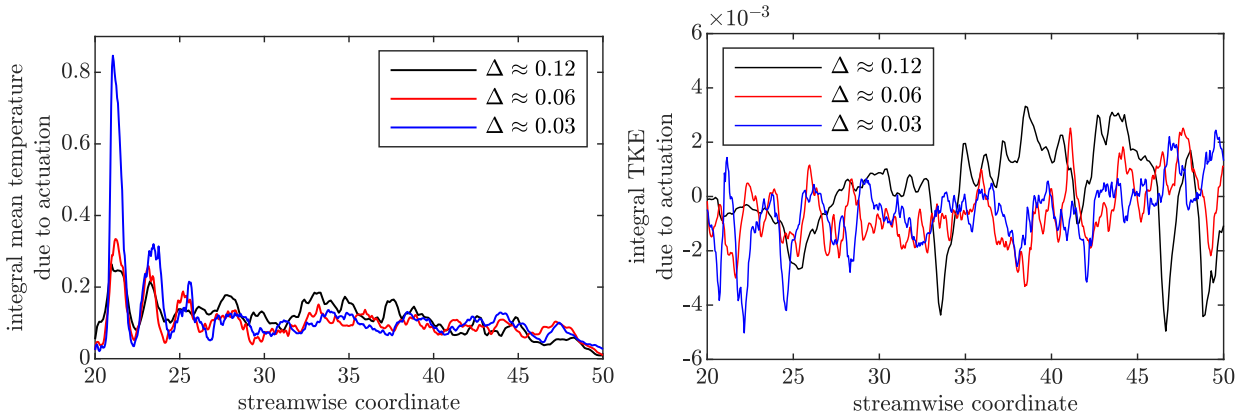

(b) Actuation with baseline subtracted

Figure 15. Spanwise-average temperature and turbulent kinetic energy after 12 actuation periods, integrated over wall-normal distance.

Acknowledgments

The experimental work and LES study are supported by ONR awards N00014-19-1-2207 (OSU) and N00014-20-1-2311 (Caltech/UCSD/Cascade), respectively, under the supervision of Dr. Steve Martens. The LES calculations were carried out on the "Onyx" Cray XC40/50 system in ERDC DSRC, using allocations provided by DoD HPCMP. The authors would like to thank Dr. Michael Emory of Cascade Technologies for his CAD expertise and key contributions to the computational domain construction.

References

[1]Brown, C. A., "Acoustics of excited jets—a historical perspective," *The Journal of the Acoustical Society of America*, Vol. 118, No. 3, 2005, pp. 1863–1863.

[2]Henderson, B., "Fifty Years of Fluidic Injection for Jet Noise Reduction," *International Journal of Aeroacoustics*, Vol. 9, No. 1, 2010, pp. 91–122.

[3]Heeb, N., Munday, D., Gutmark, E., Liu, J., and Kailasanath, K., "Supersonic Jet Noise Reduction by Chevrons Enhanced with Fluidic Injection," *40th Fluid Dynamics Conference and Exhibit*, American Institute of Aeronautics and Astronautics, 2010.

[4]Henderson, B. and Bridges, J., "An MDOE Investigation of Chevrons for Supersonic Jet Noise Reduction," *16th AIAA/CEAS Aeroacoustics Conference*, American Institute of Aeronautics and Astronautics, 2010.

[5]Bridges, J., Wernet, M., and Frate, F., "PIV Measurements of Chevrons on F400-Series Tactical Aircraft Nozzle Model," *49th AIAA Aerospace Sciences Meeting including the New Horizons Forum and Aerospace Exposition*, American Institute of Aeronautics and Astronautics, 2011.

[6]Greska, B., Krothapalli, A., Seiner, J., Jansen, B., and Ukeiley, L., "The Effects of Microjet Injection on an F404 Jet Engine," *11th AIAA/CEAS Aeroacoustics Conference*, American Institute of Aeronautics and Astronautics, 2005.

[7]Cattafesta, L. N. and Sheplak, M., "Actuators for Active Flow Control," *Annual Review of Fluid Mechanics*, Vol. 43, No. 1, 2011, pp. 247–272.

[8]Samimy, M., Kim, J. H., Kastner, J., Adamovich, I., , and Utkin, Y., "Active Control of High-Speed and High-Reynolds-Number Jets Using Plasma Actuators," *J. Fluid Mech.*, Vol. 578, 2007, pp. 305–330.

[9]Utkin, Y. G., Keshav, S., Kim, J.-H., Kastner, J., Adamovich, I. V., and Samimy, M., "Development and use of localized arc filament plasma actuators for high-speed flow control," *Journal of Physics D: Applied Physics*, Vol. 40, No. 3, 2007, pp. 685–694.

[10]Kleinman, R., Bodony, D., and Freund, J., "Numerical Modeling of Plasma Actuators in High Speed Jets," *15th AIAA/CEAS Aeroacoustics Conference (30th AIAA Aeroacoustics Conference)*, American Institute of Aeronautics and Astronautics, 2009.

[11]Kim, J., Bodony, D., and Freund, J., "LES Investigation of a Mach 1.3 Jet With and Without Plasma Actuators," *47th AIAA Aerospace Sciences Meeting including The New Horizons Forum and Aerospace Exposition*, American Institute of Aeronautics and Astronautics, 2009.

[12]Esfahani, A., Webb, N., and Samimy, M., "Coupling Modes in Supersonic Twin Rectangular Jets," AIAA paper 2021-1292, 2021.

[13]Samimy, M., Webb, N., and Crawley, M., "Excitation of Free Shear-Layer Instabilities for High-Speed Flow Control," *AIAA J.*, Vol. 56, No. 5, 2018, pp. 1770–1791.

[14]Samimy, M., Kearney-Fischer, M., , and Kim, J. H., "High-Speed and High-Reynolds-Number Jet Control Using Localized Arc Filament Plasma Actuators," *J. Propulsion and Power*, Vol. 28, No. 2, 2012, pp. 269–280.

[15]Hahn, C., Kearney-Fischer, M., , and Samimy, M., "On Factors Influencing Arc Filament Plasma Actuator Performance in Control of High Speed Jets," *Experiments in Fluids*, Vol. 51, 2011, pp. 1591–1603.

[16]Weatherill, N., "Delaunay triangulation in computational fluid dynamics," *Computers & Mathematics with Applications*, Vol. 24, No. 5, 1992, pp. 129–150.

[17]Du, Q., Faber, V., and Gunzburger, M., "Centroidal Voronoi tessellations: applications and algorithms," *SIAM review*, Vol. 41, No. 4, 1999, pp. 637–676.

[18]Brès, G. A., Ham, F. E., Nichols, J. W., and Lele, S. K., "Unstructured Large Eddy Simulations of Supersonic Jets," *AIAA J.*, Vol. 55, No. 4, 2017, pp. 1164–1184.

[19]Brès, G. A., Jordan, P., Jaunet, V., Le Rallic, M., Cavalieri, A. V. G., Towne, A., Lele, S. K., Colonius, T., and Schmidt, O. T., "Importance of the nozzle-exit boundary-layer state in subsonic turbulent jets," *J. Fluid Mech.*, Vol. 851, 2018, pp. 83–124.

[20]Brès, G. A., Bose, S. T., Emory, M., Ham, F. E., Schmidt, O. T., Rigas, G., and Colonius, T., "Large eddy simulations of co-annular turbulent jet using a Voronoi-based mesh generation framework," AIAA paper 2018-3302, 2018.

[21]Brès, G. A., Towne, A., and Lele, S. K., "Investigating the effects of temperature non-uniformity on supersonic jet noise with large-eddy simulation," AIAA paper 2019-2730, 2019.

[22]Freund, J. B., "Proposed Inflow/Outflow Boundary Condition for Direct Computation of Aerodynamic Sound," *AIAA J.*, Vol. 35, No. 4, 1997, pp. 740–742.

[23]Mani, A., "Analysis and optimization of numerical sponge layers as a nonreflective boundary treatment," *Journal of Computational Physics*, Vol. 231, 2012, pp. 704–716.

[24]Vreman, A., "An eddy-viscosity subgrid-scale model for turbulent shear flow: Algebraic theory and applications," *Physics of Fluids*, Vol. 16, Jan 2004, pp. 3670–3681.

[25]Kawai, S. and Larsson, J., "Wall-modeling in large eddy simulation: Length scales, grid resolution, and accuracy," *Phys. Fluids*, Vol. 24, 2012, pp. 015105.

[26]Larsson, J., Kawai, S., Bodart, J., and Bermejo-Moreno, I., "Large eddy simulation with modeled wall-stress: recent progress and future directions," *JSME Mech. Eng. Reviews*, Vol. 3, 2016.

[27]Bose, S. T. and Park, G. I., "Wall-Modeled Large-Eddy Simulation for Complex Turbulent Flows," *Annual Review of Fluid Mechanics*, Vol. 50, 2018, pp. 535–561.

[28]Lockard, D. P., "An efficient, two-dimensional implementation of the Ffowcs Williams and Hawkings equation," *J. Sound Vib.*, Vol. 229, 2000, pp. 897–911.

[29]Ffowcs Williams, J. E. and Hawkings, D. L., "Sound generation by turbulence and surfaces in arbitrary motion," *Philosophical Transactions of the Royal Society of London. Series A, Mathematical and Physical Sciences*, Vol. 264, 1969, pp. 321–342.

[30]Shur, M. L., Spalart, P. R., and Strelets, M. K., "Noise prediction for increasingly complex jets. Part I: Methods and tests," *Int. J. Aeroacoust.*, Vol. 4, No. 3-4, 2005, pp. 213–246.